www.elsevier.com/locate/memsci

Nanoporous organosilica membrane for water desalination: Theoretical study on the water transport

Yen Thien Chua, Guozhao Ji, Greg Birkett, Chun Xiang Cynthia Lin, Freddy Kleitz, Simon Smart

PII: S0376-7388(15)00132-5
DOI: http://dx.doi.org/10.1016/j.memsci.2015.01.060
Reference: MEMSCI13482

To appear in: *Journal of Membrane Science*

Received date: 27 October 2014
Revised date: 26 January 2015
Accepted date: 31 January 2015

Cite this article as: Yen Thien Chua, Guozhao Ji, Greg Birkett, Chun Xiang Cynthia Lin, Freddy Kleitz, Simon Smart, Nanoporous organosilica membrane for water desalination: Theoretical study on the water transport, *Journal of Membrane Science,* http://dx.doi.org/10.1016/j.memsci.2015.01.060

Nanoporous Organosilica Membrane for Water Desalination: Theoretical study on the water transport

Yen Thien Chua[a], Guozhao Ji[a], Greg Birkett[a], Chun Xiang Cynthia Lin[b], Freddy Kleitz[c], Simon Smart[a*]

[a]*The University of Queensland, School of Chemical Engineering, Brisbane, St Lucia, QLD 4072, Australia.*

[b]*The University of Queensland, Australian Institute of Bioengineering and Nanotechnology, Brisbane, St Lucia, QLD 4072, Australia.*

[c]*Department of Chemistry, 1045 Avenue de la Médecine, Université Laval, Québec, G1V 0A6 (QC), Canada*

*Corresponding author. Tel.: + 61 7 336 58591. *E-mail address: s.smart@uq.edu.au*

Abstract

An unconventional nanoporous organosilica membrane has been tested in a vacuum membrane distillation (MD) process for water desalination. We propose a modified approach to understand the transport mechanism of water molecules through the nanopores of this membrane. The modified approach stems from the fact that the membrane has a hydrophilic surface (contact angle < 90°) and so capillary pressure, which draws liquid water into the nanopore, must be considered when establishing the mathematical model. However, increased friction arising from the dramatic increase in shear viscosity of water in nano-confined spaces balances the capillary flow against the evaporative mass transport to avoid pore wetting. Notably, the liquid/vapour interface is no longer formed at the pore entrance as with a conventional hydrophobic membrane, but rather exists deeper in the pore channel as a consequence of capillary pressure. This was backed by experimental observations (no pore wetting) and SEM evidence which showed salt nucleation and growth existed only on the membrane surface, and did not infiltrate the membrane support layers. The impacts of pore size, membrane thickness, substrate thickness, concentration polarization, porosity, and contact angle on water flux and pore intrusion depth were tested using the model. Pore size was the most influential parameter with an > 80% increase in permeation flux if the pore size increased from 2 to 3 nm at 60 °C. However, pore wetting is expected if d_p > 3.4 nm, particularly at low temperatures where the slower evaporation rate promoted greater pore intrusion. Concentration polarization was shown to be negligible which agreed well with experimentally observed water fluxes which remained relatively constant despite feed salinity increasing from 0 to 150 g L^{-1}. Lastly, the membrane hydrophilicity was found to impact on water flux and pore intrusion in a complex relationship with pore size. Ultimately, hydrophilic pores less than 3 nm in diameter offer a good combination of good water flux and minimal water intrusion suggesting that ordered mesoporous organosilica membranes have potential in MD applications.

Key words: membrane distillation, organosilica membrane, nano-confined viscosity

1. Introduction

Membrane distillation (MD) is a promising process for water desalination owing to its compact design and ability to process highly concentrated brines. It is a combined process that uses both thermal energy and membranes to produce fresh water and it has the potential to overcome some of the bottlenecks of conventional processes. Compared to traditional distillation, MD operates with a smaller vapour space, reducing unit operation size and works well with lower feed temperatures < 90 °C allowing low grade / waste heat to be utilized [1]. Furthermore, MD does not require extreme pressures of the reverse osmosis process [2], and is therefore able to treat highly concentrated brine solutions up to 300 g L^{-1}[3]. Many desalination studies that utilize MD have been reported using hydrophobic, polymeric membranes (e.g. PVDF, PTFE etc.) with average pore size of 0.1 – 1.0 μm [4]. In such a system, a liquid/vapour interface or 'meniscus' is formed at the pore entrance, wherein only water will vaporize and transport across the membrane, leaving behind the non-volatile salts. The formation of this meniscus requires a hydrophobic membrane surface and that the transmembrane pressure is less than liquid entry pressure (LEP), (where LEP is expressed as $\Delta P = -2B\gamma_l \cos\theta / r_{max}$) a derivation from the Young-Laplace equation [5]. Should the transmembrane pressure exceed the LEP, liquid water will enter and then fill the pores (referred to as pore wetting), which renders the membrane incapable of separation. Typical performance requirements for MD membranes include a narrow pore size distribution, sufficient hydrophobicity, low tortuosity, high porosity, low thermal conductivity, good thermal stability and high fouling resistance [6]. As a result, most of the MD literature has focussed on increasing hydrophobicity, thermal stability and anti-fouling strategies [7-11].

Models for the transport mechanisms for different MD configurations, such as direct contact MD, air gap MD, sweep gas MD and vacuum MD, have been widely reported [10, 12-16]. In particular, vacuum MD (VMD) provides the highest water flux, establishing the highest vapour pressure gradient for a given operating temperature [6]. Unfortunately, VMD typically requires an external condenser and vacuum pump, which might increase the operating cost, although other options are available [17]. The

larger transmembrane pressure in turn also implies a greater risk of pore wetting. Several groups have extensively studied the effect of operating parameters to the membrane performance [13, 14, 18-20]. For example, Imdakm and co-workers investigated the effect of membrane pore interconnectivity on the permeate flux by using Monte-Carlo simulations [15], whereas Soukane and co-workers developed a model based on ballistic transport at the pore scale for VMD. Notably, there is no reported work using a hydrophilic, nanoporous membrane for study of transport mechanisms for a membrane with pore sizes smaller than 5 nm. Models do exist for liquid permeation in porous media for pores in this size range offering useful insight both from a mass transfer [21] and molecular dynamics perspective [22]. However, these either utilize surface diffusion or are computationally expensive, respectively which can hinder their applicability, especially under vacuum or non-isothermal conditions and there exists scope for a new approach. Our previous work described the application of a nanoporous, organosilica membrane in water desalination using VMD [23]. The membrane revealed promising water permeation fluxes and yet was unconventional where it exhibited: (1) much smaller pores (~ 2 nm) than the commonly tested polymeric membranes; (2) did not show any decline in permeation flux with the increment of salt concentration of the feed solution up to 150 g L^{-1}; and (3) no pore wetting was observed even though the membrane surface was not hydrophobic (contact angle < 90 °).

The advantages of our membrane come from its narrow pore size distribution, the combined benefits of hybrid organic and inorganic materials and thin active layer. The nanoporous membrane was prepared using the evaporation-induced self-assembly (EISA) pathway in the presence of a triblock copolymer surfactant as structure-directing agent, being the most versatile method thus far for producing thin mesoporous films [24, 25]. To accommodate the requirements of membrane properties in VMD, we selected 1, 2-bis(triethoxysilyl)ethane as the organosilica precursor for the membrane framework. The alkyl group bridging two silicon species within the matrix was reported to improve the hydrothermal stability of such hybrid silica membrane (preventing the enlargement of the pore or the densification of small pores), as well as providing some stress relaxation (reducing macroscopic cracking as observed in pure silica membranes) [26].

However, the organosilica membrane is not entirely hydrophobic due to the existence of silanol groups and the incorporation of alkyl species within the matrix instead of dangling on the pore walls (as in the case of post-grafting method). Thus, the intrusion of water into the pore channel in accordance to Hagen-Poiseuille equation is highly possible, which leads to the question of the contribution of water capillary pressure in hydrophilic pore channels. Therefore, a theoretical examination of likely transport mechanisms for our membrane is necessary. The Lucas-Washburn equation is widely used in studying the capillary rise of water in the absence of gravitational field but its implementation in nanopores (microfluidics and nanofluidics) requires some modifications [27-30]. Another question that arises relates to the behaviour of water in nanoconfined spaces, in particular, to what extent is it valid to assume the continuum hydrodynamic properties of water hold, when examined in a nano-sized space. Ortiz-Young and co-workers performed experiments using AFM on the change of water shear viscosity in a confined space and reported a great increase of the viscous shear forces of nanoconfined water near hydrophilic surfaces compared to bulk water [31]. This information is particularly meaningful in explaining the water transport phenomena in our unconventional membrane. This contribution aims to assess the water transport in the confined nanopores (pore size ~ 2 nm) of the unconventional membrane by using a simple modelling approach followed by identifying future avenues of fundamental MD research based on the results.

2. Experimental

Desalination tests were conducted with an organosilica membrane using a continuous flow system (Figure S1) of VMD as reported in our previous work [23]. The membrane module consists of a tubular membrane with feed solution was being transported into the tube lumen and vacuum was applied at the shell side. The tests were carried out at varying feed temperature of 20, 40 and 60 °C and sodium chloride solution with various concentrations (10, 35, 50, 75, 150 g L^{-1} of NaCl). The permeate flux through the membrane, J (L m^{-2} h^{-1}) was calculated by $J = (1/A)\cdot(dm/dt)$, where m is the mass of permeate collected, A as the membrane tube active area and t is the time of permeation test. Salt rejection, R (%) of the membrane was calculated by the following equation: $R = (C_f - C_p)/C_f \times 100\%$, where C_f and C_p were the feed and permeate concentrations (wt %), respectively.

The substrate porosity was measured using a mercury porosimeter (Micromeritics, AutoPore IV 9500). The obtained mercury intrusion volume was then used to calculate the porosity of the material by $(\rho_S \times V_S)/(1+\rho_S \times V_S)$, where ρ_S (g cm^{-3}) is the material's density obtained from a gas pycnometer (Micromeritics, Accupyc II 1340) and V_S (mL g^{-1}) is the mercury intrusion volume. Surface wettability of the organosilica film coated on glass slide was examined by sessile drop contact angle measurement. A water drop of about 1 μL on the surface at 10 different points was recorded using a contact angle system (Dataphysics, OCA20). The morphology of post-testing membrane was inspected using scanning electron microscopy (SEM). A JEOL JSM-6610 microscope at an accelerating voltage of 15 kV with electron source of LaB6 gun was used to perform the analysis on the sample. Prior to SEM analysis, the sample was coated with Iridium at sputtering current of 15 mA for 200 s.

3. Mathematical model of heat and mass transfer for water transport

In a typical VMD process using a hydrophobic membrane, a liquid/vapour interface is formed at the pore entrance as shown in Figure 1. This process involves both heat and mass transfer and has both thermal and concentration boundary layers with thickness δf_t and δf_c, respectively. Heat loss across the thermal boundary layer determines the water flux, owing to the evaporation rate depending on the feed side temperature at the membrane surface, Tf_m. With the phase change of water, this gives the difference of water vapour pressure, P_{vp} from the permeate pressure P_p. Since this separation process is dealing with aqueous phase and non-volatile salt components, the salt concentration C_{Bm} on the membrane phase increases with the evaporation of water (water concentration, C_{Am} is assumed to remain constant), forming a boundary layer of concentration polarization. Both thermal and concentration polarization affect the membrane flux and the rate limiting step for our unconventional membrane is yet to be determined.

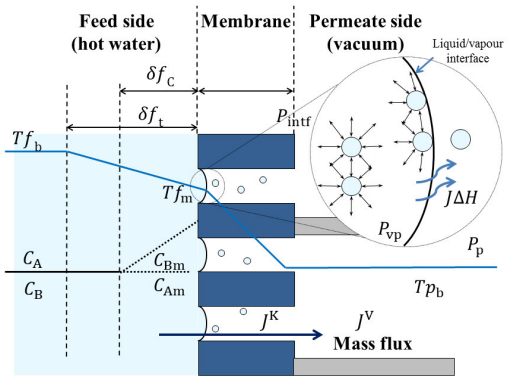

Figure 1: Schematic diagram of heat and mass transfer in VMD with thickness of membrane (navy blue), substrate (grey) and the thermal and concentration boundary layers (not to scale).

The nanoporous membrane system in this study is an asymmetric configuration with a thin active layer on a porous ceramic substrate. Liquid is fed at the feed side, whilst at the permeate side, the transport of evaporated water vapour through the membrane pore channels and then the underlying substrate is considered as gas phase transport. The active layer of the membrane is comprised of mesopores, which are smaller than the typical pore sizes encountered in VMD [13] and larger than those encountered in pervaporation [32]. A mathematical model to simulate and validate the performance of the membrane in VMD was constructed using the following assumptions:

- the system is in steady-state
- only heat conduction is considered at the feed side liquid boundary layer
- only heat conduction is considered across the membrane
- interconnectivity of pore channels is not considered

From the mass transfer perspective, the entire system is divided into four main regions as shown in Figure 2:

(i) water transport from the bulk to the membrane pore entrance;

(ii) water transport in liquid phase from the pore entrance to the liquid/vapour interface;

(iii) transport of water vapour molecules from the liquid/vapour interface to the pore exit; and

(iv) transport of water vapour molecules from the pore exit, through the macroporous alumina substrate to vapour bulk under vacuum.

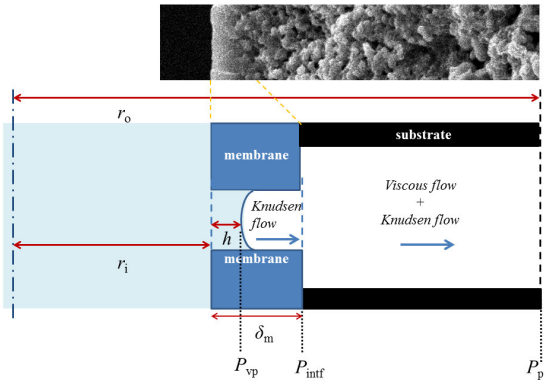

Figure 2 Schematic diagram of the mass transfer within the nanopores across the membrane to its substrate

3.1 Liquid phase flow through membrane pores

Since the membrane in this study is hydrophilic (Figure S2), it is expected that water will penetrate the membrane pores. However, the position of the liquid/vapour interface within the nanopore (or perhaps the macroporous support) is an unanswered question. Experimental observations from the previous work suggest that the membrane did not exhibit any pore wetting (i.e. the liquid water or crystallized salt was not observed on the permeate side of the membrane) even when tested for highly concentrated brines and higher feed temperatures of up to 60 °C. Water continuously evaporates from the interface due to the vapour pressure gradient. As there is no pore wetting observed, this implies the liquid/vapour interface lies at the position where the evaporation rate is in equilibrium with the liquid entry rate.

The Lucas-Washburn equation can be implemented to describe the capillary forces in nanopores, which has been widely used in microfluidics and nanofluidics. However, water properties have been found to greatly differ in confined space compared to the continuum dynamic flow regime, particularly in that the shear viscosity of water in a confined space (< 1 nm) could be in orders of magnitude higher than the classical continuum theory (about 70 Pa.s at room temperature for a silica surface) [31, 33]. Since the validity of macroscopic capillarity has been proven to be applicable down to meso- and nanoscale [29, 30], the Lucas-Washburn equation (eqn (1)) is used to express the capillary phenomena of water filling into the hydrophilic pore by defining the rise of liquid/vapour interface $h(t)$ over time t [27],

$$h(t) = \left(\frac{\gamma_l r_p \cos\theta}{2\eta_l} \right)^{1/2} \sqrt{t} \quad (1)$$

where, γ_l is liquid surface tension, r_p is pore radius, θ the contact angle between the liquid/vapour interface and the wall and η_l is the shear viscosity of liquid [31]. Solving the differential eqn (1) will give a term (eqn 2) expressed in volumetric flux as,

$$J_{vol} = \frac{dh}{dt} = \frac{\gamma_l r_p \cos\theta}{4h\eta_l} \quad (2)$$

3.2 Gas phase flow in the active membrane layer

The transport mechanisms of gas or vapour within a porous material are routinely described by viscous flow, Knudsen flow and activated diffusion depending on temperature, pressure and membrane pore size [34]. To investigate the transport of water vapour across the organosilica membrane, it is necessary to find the mean free path, λ, of the molecule within the membrane pores, which can be derived from eqn (3),

$$\lambda = \frac{k_B T}{\sqrt{2}\pi \overline{P} \sigma_i^2} \quad (3)$$

where, k_B is the Boltzmann constant, σ is the collision diameter (0.2641 nm for water vapour), $\overline{P}$ is the mean pressure within the membrane pores which is simply approximated by the average of vapour pressure and permeate pressure, and T is absolute temperature.

The calculated mean free path as a function of temperature for a water vapour molecule is depicted in Figure 3.

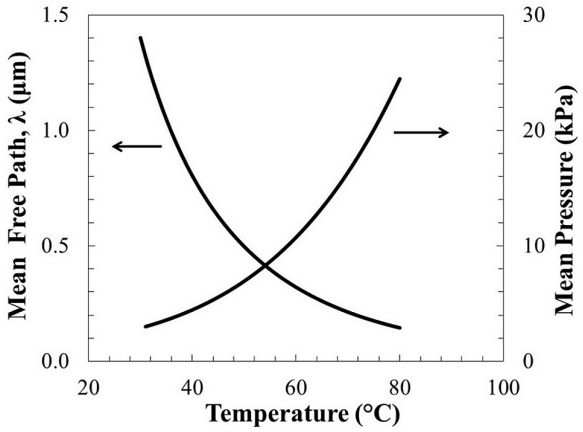

Figure 3 Mean free path of water vapour molecules and mean pressure at different temperature

As shown in Figure 3, the value of mean free path is more than two magnitudes greater than the pore size of 2 nm, which implies that the vapour transportation in the membrane pores is in the Knudsen regime or activated diffusion regime. The pore size boundary between Knudsen flow and activated diffusion was firstly defined by Thornton et al. [35]; as when the molecule's kinetic energy is less than the absolute value of the pore wall potential, the transport is more likely to be governed by activated diffusion rather than Knudsen flow. Therefore, the potential distribution of a water vapour molecule in a 2 nm pore was calculated by using Lennard-Jones potential (Figure 4). The Lennard Jones parameters used in this work are listed in Table 1. The pores are assumed to be cylindrical and the pore wall is formed by silicon and carbon atoms with equal and uniform distribution. The interaction of the vapour molecule with the pore wall is a minimum (potential energy of 1.17×10^{-20} J) at a distance about 0.142 nm from the pore wall.

Table 1 Lennard Jones parameters used in this work

Parameter	Si	C	H_2O
σ(nm)	0.28	0.34	0.2641
ε/k_B (K)	492.7	36	809.1

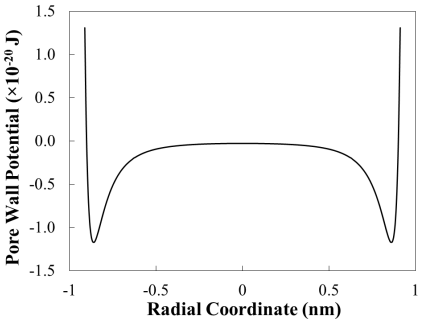

Figure 4 Potential distribution of a water vapour molecule in a 2 nm organosilica cylindrical pore given that the 0 coordinate is the center of the pore

To determine the kinetic energy of a vapour molecule, it can be estimated by the classical kinetic theory by using eqn (4),

$$E_k = \frac{i}{2} kT \tag{4}$$

where, i is the freedom of the molecule, being 6 for H_2O. In this work, the experiment was carried out from 20 °C to 60 °C, which gives the kinetic energy of 1.214×10^{-20} J to 1.379×10^{-20} J. According to Thornton et al.'s definition, the vapour molecule kinetic energy is greater than the pore wall potential energy, implying that 2 nm is greater than the minimum pore size for Knudsen flow. Therefore, the transport of vapour molecule across the top layer is still considered to be Knudsen flow, as governed by eqn (5).

$$J^K = -\frac{2}{3}\frac{\varepsilon r_p}{\tau}\sqrt{\frac{8}{\pi RTM_i}}\frac{dP}{dr} \tag{5}$$

where, J^K is the flux in Knudsen flow, ε the porosity of the membrane, τ is pore tortuosity, M is the molecular weight of the transported species i. Considering pressure at feed side as the vapour pressure, P_{vp}, and the pressure at the interface of membrane and substrate as, P_{if}, the flux across a membrane of thickness δ_m can be determined from eqn (5) as,

$$J^K = \frac{2}{3}\frac{\varepsilon r_p}{\tau}\sqrt{\frac{8}{\pi RTM_i}}\frac{P_{vp} - P_{if}}{\delta_m - h} \tag{6}$$

The vapour pressure of the NaCl solution, P_{vp} as a function of temperature and concentration can be calculated using the thermodynamic equations as reported by Sparrow et al. from 0 °C ≤ T ≤ 150 °C [36].

3.3 Mass transfer in the membrane support layer

From the data provided by manufacturer, the average pore size of the substrate is ~ 2 μm. Since the pore size is in the same magnitude of mean free path λ, so the flow must contain both viscous and Knudsen flow. A model superimposing Knudsen and viscous contributions is appropriate to describe the transport mechanism in the substrate. Assuming cylindrical pores, in the spirit of Dusty Gas Model (DGM) [37-39], the flow rate through the substrate can be expressed as,

$$F = -\frac{\varepsilon}{\tau}\left[\frac{97 r_s}{R\sqrt{MT}}\frac{\mathrm{d}P}{\mathrm{d}r} + \frac{r_s^{\,2} P}{8\eta_v RT}\frac{\mathrm{d}P}{\mathrm{d}r}\right] 2\pi r L \tag{7}$$

where, L being the length of membrane, η_v being the viscosity of water vapour and r_s being the pore radius of substrate. In a tubular substrate, the flux is not constant due to the fact that the flow is in the radial direction, but the flow rate remains constant. We will treat the flux at inner radius as the substrate flux as follows,

$$J = -\frac{\varepsilon}{\tau r_i \ln(r_o/r_i)}\left[\frac{97 r_s}{R\sqrt{MT}}\left(P_{if} - P_p\right) + \frac{r_s^{\,2} P}{16\eta RT}\left(P_{if}^{\,2} - P_p^{\,2}\right)\right] \tag{8}$$

where, r_i is the inner radius of substrate and P_p being the permeate side pressure.

Other than this, we consider the pressure drop in our membrane module system, in which the vacuum pump system is located at a certain distance from our test rig. The permeate pressure is a function of flow rate, pipe radius and pipe length, whereas the pressure in the vacuum line follows the Hagen-Poiseuille equation [40, 41],

$$\frac{\mathrm{d}P}{\mathrm{d}l} = -\frac{8\eta_v FRT}{\pi r_{pp}^{\,4} P} \tag{9}$$

$$\int_{P_{lm}}^{P_p} P\,\mathrm{d}P = -\frac{8\eta_v FRT}{\pi r_{pp}^{\,4}} \int_0^{L_p} \mathrm{d}l \tag{10}$$

where, F is permeate flow rate, r_{pp} being radius of vacuum line, P_{lm} being the pressure of the vacuum pump and L_p as the length of the vacuum line from the rig to the pump.

$$P_p = \sqrt{\frac{16\eta_v FRT}{\pi r^4} l + P_{lm}^{\,2}} \tag{11}$$

3.4 Heat transfer

As MD is a thermal process, heat transfer across the membrane involves:

(i) heat transport through the feed boundary layer with thickness δf_t (Figure 1),

(ii) heat transport through the membrane and substrate,

(iii) heat transport through the permeate boundary layer.

Due to the application of vacuum at the permeate side in VMD, the conductive heat loss across the permeate boundary layer can be neglected. A two-dimensional model has been designed with heat transfer in the bulk liquid along the membrane longitudinal direction z and radial coordinate r from the tube center ($r = 0$),

$$\frac{1}{r}\frac{\partial}{\partial r}\left(r\rho_l u_r T\right)+\frac{\partial}{\partial z}\left(\rho_l u_z T\right)=\frac{k_l}{C_{p,l}}\left[\frac{1}{r}\frac{\partial}{\partial r}\left(r\frac{\partial T}{\partial r}\right)+\frac{\partial}{\partial z}\left(\frac{\partial T}{\partial z}\right)\right] \tag{12}$$

where, k_l is thermal conductivity of liquid phase and $C_{p,l}$ as the specific heat of water. The heat transfer at the interface of liquid and membrane is expressed as,

$$\frac{1}{r}\frac{\partial}{\partial r}\left(r\rho_l u_r T\right)+\frac{\partial}{\partial z}\left(\rho_l u_z T\right)=\frac{k_l}{C_{p,l}}\left[\frac{1}{r}\frac{\partial}{\partial r}\left(r\frac{\partial T}{\partial r}\right)+\frac{\partial}{\partial z}\left(\frac{\partial T}{\partial z}\right)\right]-\frac{Q}{C_{p,l}}\frac{\partial A}{\partial V} \tag{13}$$

Heat loss Q can be derived by,

$$Q=\Delta H\cdot J_m \tag{14}$$

where ΔH is the enthalpy change of unit mass and J_m is the mass flux,

$$J_m=\rho\cdot u_r \tag{15}$$

In the substrate, the flow in the longitudinal direction z is negligible in relative to the flow in radial direction r. Thus, heat transfer across the substrate during water vaporization could be simplified into one-dimensional equation as,

$$\frac{1}{r}\frac{\partial}{\partial r}\left(r\rho_v u_{r,v} T\right)=\frac{k_s}{C_{p,v}}\frac{1}{r}\frac{\partial}{\partial r}\left(r\frac{\partial T}{\partial r}\right) \tag{16}$$

And substituting Eqn (15) into Eqn (16) gives,

$$\frac{1}{r}\frac{\partial}{\partial r}\left(rJ_m T\right)=\frac{k_s}{C_{p,v}}\frac{1}{r}\frac{\partial}{\partial r}\left(r\frac{\partial T}{\partial r}\right) \tag{17}$$

where, $u_{r,v}$ is the radial velocity in vapour phase, k_s is the thermal conductivity of vapour and substrate and $C_{p,v}$ is the specific heat of vapour.

4. Results and Discussion

The properties of the organosilica membrane are listed in Table 2 with a narrow pore size distribution at around 2 nm as reported elsewhere [23]. This information was implemented in the mathematical model to data fit the experimental results. Contact angle measurement (Figure S2) suggests the surface of organosilica membrane is hydrophilic.

Table 2 Properties of organosilica membrane and the alumina substrate

Properties	
BET surface area, $m^2\ g^{-1}$	310
Total pore volume (V_p), $cm^3\ g^{-1}$	0.18
Pore width (d_p), nm	2
Membrane thickness (δ_m), μm	1
Substrate manufacturer	PALL
Substrate material	Al_2O_3
Substrate inner diameter, mm	7
Substrate outer diameter, mm	10
Substrate porosity, %	25.7

The morphology of the organosilica membrane before and after the desalination tests was studied by SEM as shown in Figure 5. The fresh membrane (Figure 5 (a)) has a smooth surface whereas the tested membrane was found to have bundles of salt crystals growing on the organosilica surface. Figure 5 (d) shows the cross-sectional view of the organosilica membrane and the substrate. No salt crystals are observed on the alumina substrate, as shown in the enlarged boundary layer of the smaller alumina particles and larger alumina particles. It is quite interesting that the direction of growth and nucleation of the salt crystals was upward from the organosilica to air but not growing inside the membrane matrix. This could be explained by the nucleation of the salt ions happening only when the membrane is exposed to air, after desalination test has been stopped. It also provides strong evidence that the saline feed water did not pass through the active top layer of the membrane into the membrane substrate, and the capillary/evaporation equilibrium is reached inside the membrane layer.

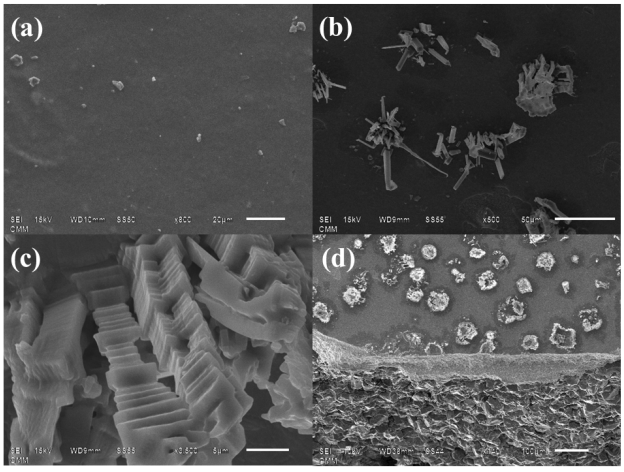

Figure 5 SEM images of the (a) fresh membrane before testing and (b) membrane after testing in desalination; (c) enlarged views of salt crystals growing from underneath membrane in island forms; (d) cross-sectional view of supported membrane (from top) organosilica membrane and salt crystals, titania layer, alumina substrate.

4.1 Model validation

The established mathematical model was validated with the experimental data obtained from desalination tests over a range of salt concentrations and feed temperature as presented in Figure 6 [23].

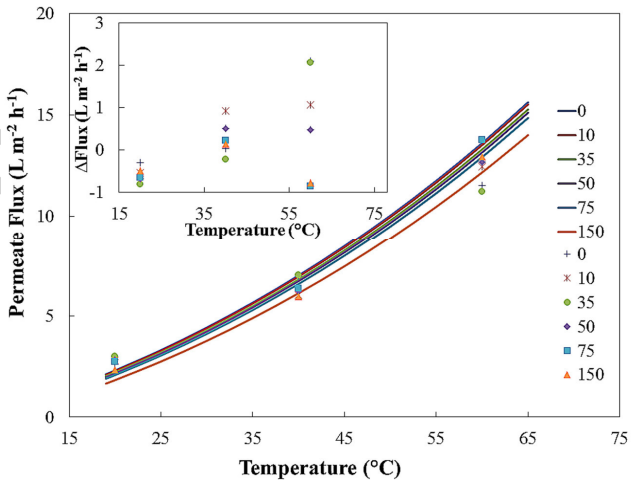

Figure 6 Plot of model fitting to the experimental data for salt concentrations from 0 to 150 g L^{-1} and temperatures from 25 – 60 °C. Symbols present the experimental data and curves represent the calculated values. Inset shows the variations of predicted values from model to the experimental data.

There are two important observations from Figure 6. The first is that the model and experimental data fit well with root mean square error below 0.78. The second is that

the effect of salt concentration on the permeate flux is not significant, contrary to the findings of other studies utilizing inorganic membranes for MD or pervaporative desalination [42]. This is predominantly governed by the minor changes in P_{vp}, and thus driving forces, that occur as a result of changes in salt concentration [36].

Integration of the Lucas-Washburn equation yields the estimated distance the liquid phase travels into the pore channel, as presented in Figure 7. For the experimental conditions used in this study, the deepest distance the salt water travels into the membrane active layer is 470 nm at feed temperature of 20 °C. This value decreases as feed temperature increases, which is attributed to an increase in the evaporation rate relative to the liquid intrusion rate. Figure 7 implies that the water intrusion rate is more dominating when the feed temperature is lower, with the liquid/vapour interface shifted further into the membrane pores. It should be noted that the membrane has a thickness of ~1 μm which correlates well with the lack of pore wetting observed. The intriguing idea here is that the intrusion of more liquid water at lower temperatures has in a sense decreased the distance the water vapour must travel in the Knudsen region of the membrane, in effect decreasing the Knudsen resistance.

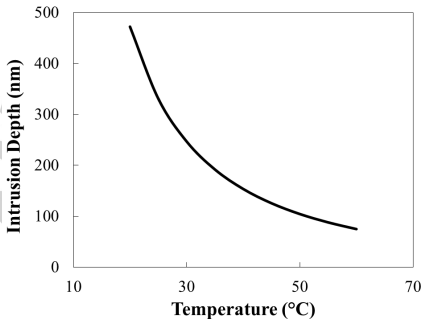

Figure 7 Water intrusion depth within a 2nm nanopore channel at varying liquid temperatures.

4.2 Temperature Polarization

The temperature values across the membrane were measured at the feed side and permeate side by K-type thermocouples and these values were used to determine the heat loss across the membrane. Figure 8 presents the heat transfer profile of the system from the tube centre (radial coordinate = 0) to the permeate side of membrane (outer surface) in a radial direction. Both of these points were experimentally measured

(indicated as data points on Figure 8) and used as inputs for the modelled temperature profile (indicated by the lines on Figure 8). As the feed temperature increases, the thermal boundary layer becomes more severe. Most of the heat loss occurs in the thermal boundary layer, which is attributed to the vaporization of water. Indeed, the Nusselt number is approximated at 3.66 for fully developed laminar flow (Re = 250) in a tube with constant surface temperature [43], which confirms that convective heat transfer away from the membrane surface is only marginally larger than conductive heat transfer through the membrane itself. At low temperature, heat loss is very limited and almost negligible, suggesting the driving force is maintained by the low vapour pressure on the permeate side by means of the vacuum pump.

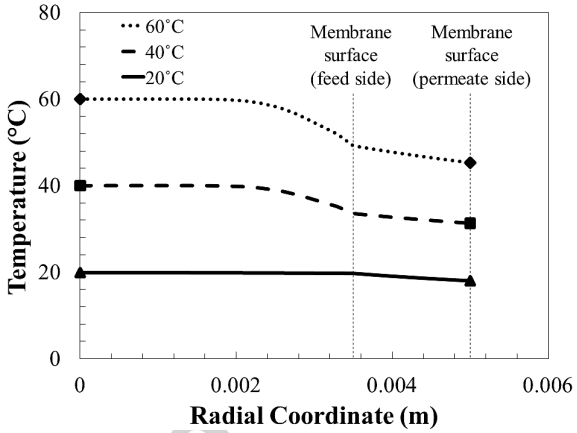

Figure 8 Heat transfer profile of the feed solution to the membrane at varying feed temperature from center of tube lumen (0 coordinate) to the permeate side of membrane (outer surface) as predicted by our model.

4.3 Concentration polarization

In MD, concentration polarisation (CP) has been found to influence membrane flux [4]. Here we are concerned with two types of concentration polarisation, namely external and internal CP. External CP occurs in the liquid phase on the membrane surface before entering the pore; whereas internal CP is defined as the concentration variation within the pore channel itself. From the macroscopic view, the flow within the membrane tube is laminar (Re = 250) which suggests the thickness of the boundary layer for external concentration polarization on the feed side (δf_c) should be further examined in line with the analysis of temperature polarization. However, in the case of external CP the Sherwood number ranges from 14-17 [43] which indicates that the convective mass transfer away from the membrane surface is more influential that the

diffusive flow through the boundary layer. This in combination with the low sensitivity of vapour pressure to salt concentration [36], explains why the external CP is not a dominating factor in the mass transport.

However, the high cross flow velocity in the bulk solution does not affect the flow within the pore. Internal concentration polarization (ICP) on the other hand may lead to either a decline in flux or built-up of salt crystals if supersaturation of the saline feed is reached. It is necessary to understand the degree of ICP in our system. Figure 9 shows the penetration of liquid into the membrane pore until the liquid/vapour interface is reached. In the radial direction, the salt concentration increases due to evaporation of water; this permeate flow drives the salt from r_1 to r_2 via advection. In the meantime, there is a diffusive flow in the opposite direction, driven by the salt concentration gradient between the pore (higher) and the bulk feed (lower) and allows the bulk concentration to be maintained in equilibrium.

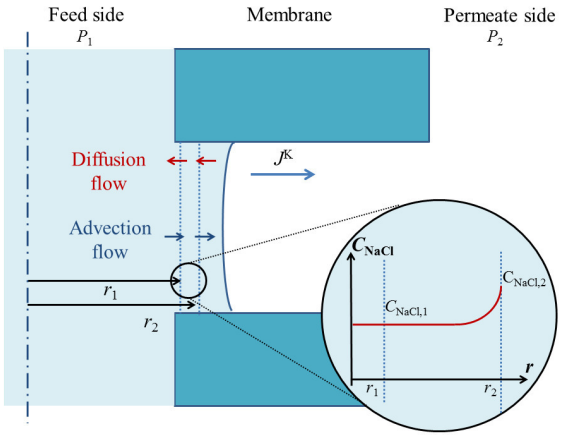

Figure 9 Internal concentration polarization inside the organosilica pore channel

Hence a mass balance for NaCl concentration can be performed,

$$Jx_2r_2 - Jx_1r_1 = D\left(\frac{\mathrm{d}c_{\mathrm{NaCl}}}{\mathrm{d}r}\right)_2 r_2 - D\left(\frac{\mathrm{d}c_{\mathrm{NaCl}}}{\mathrm{d}r}\right)_1 r_1 \tag{18}$$

where, D is diffusion coefficient of salt in water, x is the molar fraction of NaCl in water, C_{NaCl} is concentration of NaCl in water. If r_2 is approaching to r_1, eqn (18) can be re-written in derivative format as,

$$J\frac{\mathrm{d}(xr)}{\mathrm{d}r} = \frac{\mathrm{d}}{\mathrm{d}r}\left(Dr\frac{\mathrm{d}c_{\mathrm{NaCl}}}{\mathrm{d}r}\right) \tag{19}$$

If we assume the total concentration c is constant,

$$c_{\mathrm{NaCl}} = c \cdot x \tag{20}$$

$$J\frac{\mathrm{d}(xr)}{\mathrm{d}r} = Dc\frac{\mathrm{d}}{\mathrm{d}r}\left(r\frac{\mathrm{d}x}{\mathrm{d}r}\right) \tag{21}$$

$$Jx + Jr\frac{\mathrm{d}x}{\mathrm{d}r} = Dcr\frac{\mathrm{d}^2x}{\mathrm{d}r^2} + Dc\frac{\mathrm{d}x}{\mathrm{d}r} \tag{22}$$

Two boundary conditions are required to solve the second order derivative, given that

$$\begin{cases} r = r_i; x = x_0 \\ r = r_i; \dfrac{\mathrm{d}x}{\mathrm{d}r} = 0 \end{cases}$$

By solving the above equations, the ICP profile could be determined. Figure 10 represents the relationship of ΔC, where$\Delta C = C - C_0$ (C is the concentration along the intrusion depth and C_0 is the bulk concentration) to the intrusion depth at the highest salt concentration tested (150 g L^{-1} or 0.0441 mol m^{-3}) and feed temperatures of 20, 40 and 60 °C. As seen previously in Figure 10, the lowest temperature has the greatest intrusion depth due to the lower water evaporation rate. The further the liquid travels into the pore the greater the ICP. However, the real difference in the salt concentration is very small, on the order of picomoles m^{-3} compared to the bulk concentration of 0.0441 mol m^{-3}. To evaluate the sensitivity of the internal CP to temperature effects associated with back diffusion of salts, the diffusion coefficient, D, was artificially increased and decreased by 3 orders of magnitude (Figure S3). The internal CP profile with pore depth also increased and decreased by 3 orders of magnitude; however the relative change in concentration remained negligible when compared to the total bulk concentration. It is therefore appropriate to neglect the ICP within the nanopores. This correlates well the lack of that flux decline and salt crystal formation in the membrane during operation.

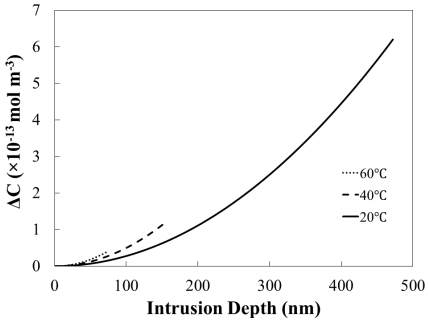

Figure 10 Profile of internal concentration polarization (ICP) in function of the depth of water intrusion in nanopores.

4.4 Effect of membrane properties

Given the fine balance between liquid intrusion and evaporation that exists within the pores, it is important to understand the effect of varying pore size, operating temperature and its likelihood to undergo pore wetting. The change of water shear viscosity with the pore size has been taken into consideration during the simulation. These values were estimated based on the reported work from Riedo's group [31, 33]. Figure 11 shows the pore size effect on the intrusion depth of pure water into the pore channel and the water permeation flux at temperature of 20, 40 and 60 °C. Water intrudes deeper into the pore channel as pore size increases. This is to be expected as the water shear viscosity sharply reduces when the pore size increases, quickly approaching bulk water viscosity. The maximum allowable pore size for this type of organosilica membrane (at this active layer thickness) is at 3.4 nm but pore wetting is very likely to occur at 20 °C. This suggests that surface modification is necessary if a larger pore size is required to enhance the membrane permeation flux. Regarding future membrane design it is significant to note that enlarging the pore size by 50 % from 2 to 3 nm provides permeation flux enhancement of approximately 82 %, 49 % and 41 % at feed temperature of 20, 40 and 60 °C, respectively.

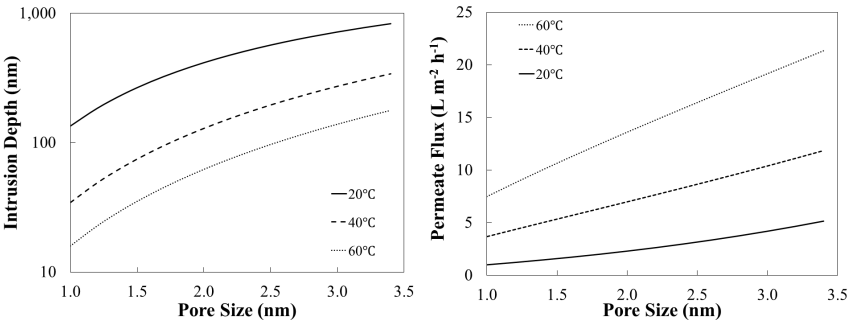

Figure 11 Effect of pore size to the liquid intrusion depth (left) and water permeation flux (right) at varying temperature

As for the membrane porosity, an increment of 50 % from 0.24 to 0.36 was found to improve the membrane water flux approximately 28 % irrespective with the change of feed temperature as can be seen in Figure 12. A 100 % improvement of membrane porosity to 0.4 may enhance the flux approximately 75 %. However, it is quite challenging to prepare a stable inorganic membrane with porosity of 0.4 as the mechanical strength of the membrane and its performance need to be balanced.

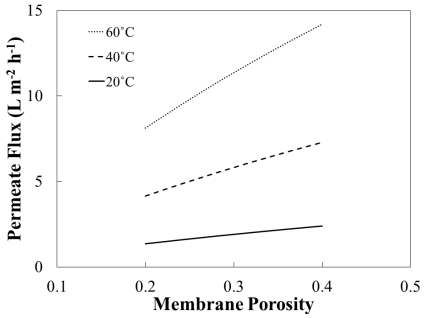

Figure 12 Effect of membrane porosity to the membrane permeation flux at varying feed temperature

Membrane thickness has a significant impact on the water permeation flux as presented in Figure 13. The flux was modelled for membranes with thicknesses from 500 nm to 3 μm. An increase of approximately 27 % in the membrane water flux is observed when decreasing the membrane thickness from 1 to 0.5 μm at a feed temperature of 60 °C. However, fabricating a 500 nm thick, defect-free organosilica membrane with ordered pore structure is quite challenging and large performance gains are unlikely to be achieved here.

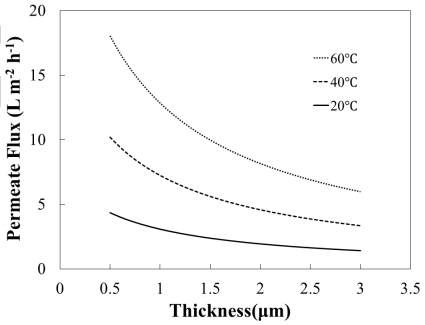

Figure 13 Effect of membrane thickness to water permeation flux

In comparison to membrane thickness, the effect of membrane support thickness on water flux is less intuitive as the primary function of the support is to provide mechanical strength. Further it is sometimes assumed that the large pore sizes of the membrane support do not significantly contribute to the overall transport resistance of the membrane, although this is not always the case [44]. Indeed, apportioning the

resistance to flux through the membrane to either the top membrane layer or the membrane support reveals that the membrane support accounts for between ~20 – 30 % of the total resistance (Table S1). This indicates it is a useful target for optimized design, although it should be noted that the support does not induce a significant pressure drop (Figure S4). Further to this Figure 14 shows that the flux could be improved approximately 15 % if the substrate thickness is reduced to 0.5 mm.

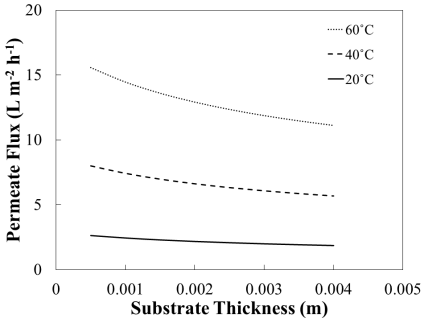

Figure 14 Effect of substrate thickness to water permeation flux at varying feed temperature

The model proposed here relies on the assumption that the liquid/vapour interface occurs at some point within the nanopore channel, specifically at the position where the evaporation rate is in equilibrium with the liquid entry rate. This is a delicate balance and necessitates a sensitivity analysis of the model parameters, as several were sourced from other studies or calibrated from experimental results. Given the importance of pore surface hydrophilicity/hydrophobicity (i.e. contact angle) in determining shear viscosity which in turn influences membrane flux and pore intrusion depth, these were further investigated with the results shown in Figure 15.

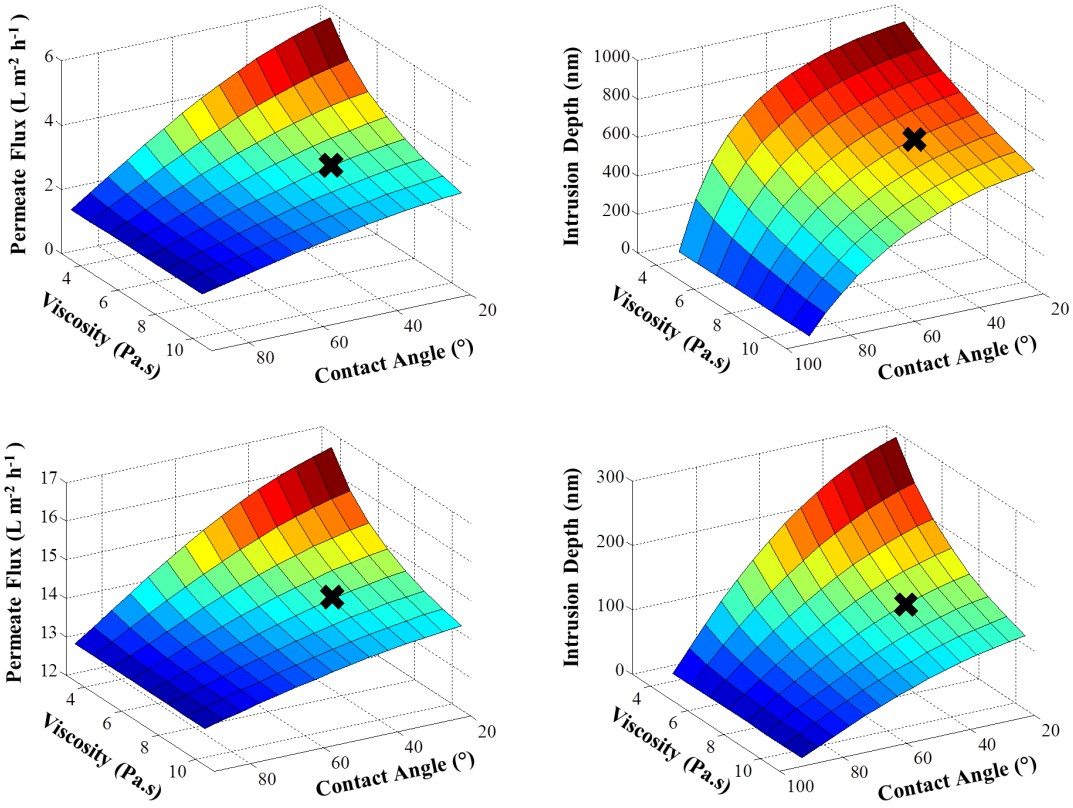

Figure 15 Effect of membrane surface hydrophilicity/hydrophobicity to water permeation flux and intrusion depth at 20 °C (top) and 60 °C (bottom). Values used in this study are marked with an X.

It is important to note here that the surfaces presented in Figure 15 are continuous only for the purposes of analysing the parameters of the model and do not represent the physical system. Rather, the intent is to examine how an inaccurate estimate of contact angle or viscosity impacts of the predicted membrane flux and pore intrusion depth. To this end the values used in our study are marked on each surface to provide a visual indication of how sensitive the model is to these parameters. The results showed that for high values of shear viscosity (e.g. > 5 Pa.s) surface hydrophilicity had minimal impact on the overall membrane flux, which decreases as contact angle increases. On the other hand, contact angle significantly impacts on both membrane flux and pore intrusion depth at low shear viscosities (e.g. < 5 Pa.s), rapidly increasing pore intrusion depth in particular. The effects here are more pronounced at lower temperatures (e.g. 20°C) as opposed to higher temperature (e.g. 60°C). Assessing the region of interest for the membrane under investigation, it is clear that the degree of uncertainty in the contact angle and shear viscosity parameters does impact on the robustness of the overall model. Indeed, for the model, the success of the membrane in avoiding pore wetting during MD operation is predicated on a value of shear viscosity for water that is several orders of magnitude greater than bulk water. There is a growing body of

experimental evidence in the literature backing this assumption [45-48]. In turn, the experimental results combined with the model developed here indirectly support the idea that the shear viscosity of water is dramatically different in a nano-confined space. Indeed, there is no other explanation for the successful operation of the membrane and absence of pore wetting without it. However, greater accuracy for both the surface hydrophobicity and shear viscosity would certainly assist in further refining the model.

5. Conclusions

In conclusion, a mathematical model was established both to describe the water transport in a hydrophilic, nanoporous VMD system and to understand the influence of the membrane properties on the separation performance. The model corroborates well with the experimental data considering the heat transfer and heat loss across the membrane, as well as the change of water vapour pressure with the salt concentration. Despite the conventional wisdom that a hydrophobic membrane is considered a mandatory criteria in MD, the hydrophilic nanoporous membrane studied does not exhibit any pore wetting. This is mainly attributed to the confinement effects of the nanopore channels, which have dramatically increased the shear viscous force of water with respect to the hydrophilic pore wall. The model showed how the liquid/vapour interface is formed within the nanopores due to the opposing 'forces' of intrusion and evaporation. Indeed, despite vast differences in salt concentration and a liquid intrusion depth of up to 470 nm, negligible internal concentration polarization is observed within the confined nanospace. Increasing the pore size slightly enhanced the permeation flux but the trade-off was the increased risk of total pore wetting of the pore channel and membrane substrate. Similarly, the model found that a thin membrane is beneficial in inducing higher flux, particularly as the greatest resistance to water permeation is the Knudsen diffusion of the water vapour through the nanochannels. Indeed, it is now possible to predict the intrusion depth using the model developed here and thereby tailor the membrane thickness to minimise this resistance. However, the more dominant factor is the heat transfer across the membrane which can be reduced by choosing to make the membrane from a material with low thermal conductivity.

Acknowledgements

The authors would like to acknowledge funding from the Australian Research Council in the form of ARC-DP 110103440. F.K. thanks NSERC (Canada) and FQRNT (Province of Québec) for the financial support. Y.C. would like to acknowledge scholarship support from The University of Queensland in the form of the UQI International Scholarship. S.S. would like to acknowledge the Queensland Government Smart Futures Fellowship. The authors also thank Diego Schmeda for the analysis of the material porosimetry. The authors acknowledge the facilities, and the scientific and technical assistance, of the Australian Microscopy & Microanalysis Research Facility at the Centre for Microscopy and Microanalysis, The University of Queensland.

References

[1] K.W. Lawson, D.R. Lloyd, Membrane distillation, Journal of Membrane Science, 124 (1997) 1-25.
[2] T. Humplik, J. Lee, S.C. O'Hern, B.A. Fellman, M.A. Baig, S.F. Hassan, M.A. Atieh, F. Rahman, T. Laoui, R. Karnik, E.N. Wang, Nanostructured materials for water desalination, Nanotechnology, 22 (2011) 1-19.
[3] M. Safavi, T. Mohammadi, High-salinity water desalination using VMD, Chemical Engineering Journal, 149 (2009) 191-195.
[4] M.S. El-Bourawi, Z. Ding, R. Ma, M. Khayet, A framework for better understanding membrane distillation separation process, Journal of Membrane Science, 285 (2006) 4-29.
[5] A.C.M. Franken, J.A.M. Nolten, M.H.V. Mulder, D. Bargeman, C.A. Smolders, Wetting criteria for the applicability of membrane distillation, Journal of Membrane Science, 33 (1987) 315-328.
[6] M. Khayet, Membranes and theoretical modeling of membrane distillation: A review, Advances in Colloid and Interface Science, 164 (2011) 56-88.
[7] S. Cerneaux, I. Struzynska, W.M. Kujawski, M. Persin, A. Larbot, Comparison of various membrane distillation methods for desalination using hydrophobic ceramic membranes, Journal of Membrane Science, 337 (2009) 55-60.
[8] M. Gryta, Fouling in direct contact membrane distillation process, Journal of Membrane Science, 325 (2008) 383-394.
[9] B. Li, K.K. Sirkar, Novel membrane and device for vacuum membrane distillation-based desalination process, Journal of Membrane Science, 257 (2005) 60-75.
[10] P. Wang, M.M. Teoh, T.-S. Chung, Morphological architecture of dual-layer hollow fiber for membrane distillation with higher desalination performance, Water Research, 45 (2011) 5489-5500.
[11] Z.D. Hendren, J. Brant, M.R. Wiesner, Surface modification of nanostructured ceramic membranes for direct contact membrane distillation, Journal of Membrane Science, 331 (2009) 1-10.
[12] C.A. Rivier, M.C. García-Payo, I.W. Marison, U. von Stockar, Separation of binary mixtures by thermostatic sweeping gas membrane distillation: I. Theory and simulations, Journal of Membrane Science, 201 (2002) 1-16.
[13] M. Khayet, T. Matsuura, Pervaporation and vacuum membrane distillation processes: Modeling and experiments, AIChE Journal, 50 (2004) 1697-1712.
[14] S. Bandini, A. Saavedra, G.C. Sarti, Vacuum membrane distillation: Experiments and modeling, AIChE Journal, 43 (1997) 398-408.

[15] A.O. Imdakm, M. Khayet, T. Matsuura, A Monte Carlo simulation model for vacuum membrane distillation process, Journal of Membrane Science, 306 (2007) 341-348.
[16] H. Chang, J.-S. Liau, C.-D. Ho, W.-H. Wang, Simulation of membrane distillation modules for desalination by developing user's model on Aspen Plus platform, Desalination, 249 (2009) 380-387.
[17] A. Hausmann, P. Sanciolo, T. Vasiljevic, M. Weeks, M. Duke, Integration of membrane distillation into heat paths of industrial processes, Chemical Engineering Journal, 211-212 (2012) 378-387.
[18] J. Zhang, J.-D. Li, M. Duke, M. Hoang, Z. Xie, A. Groth, C. Tun, S. Gray, Modelling of vacuum membrane distillation, Journal of Membrane Science, 434 (2013) 1-9.
[19] K.W. Lawson, D.R. Lloyd, Membrane distillation. I. Module design and performance evaluation using vacuum membrane distillation, Journal of Membrane Science, 120 (1996) 111-121.
[20] A. Criscuoli, M.C. Carnevale, E. Drioli, Modeling the performance of flat and capillary membrane modules in vacuum membrane distillation, Journal of Membrane Science, 447 (2013) 369-375.
[21] K.-H. Lee, S.-T. Hwang, The transport of condensible vapors through a microporous vycor glass membrane, Journal of Colloid and Interface Science, 110 (1986) 544-555.
[22] T. Yoshioka, H. Nagasawa, M. Kanezashi, T. Tsuru, Micropore Filling Phase Permeation of a Condensable Vapor in Silica Membranes: A Molecular Dynamics Study, J. Chem. Eng. Jpn., 46 (2013) 659-671.
[23] Y.T. Chua, C.X.C. Lin, F. Kleitz, X.S. Zhao, S. Smart, Nanoporous organosilica membrane for water desalination, Chemical Communications, 49 (2013) 4534-4536.
[24] D. Grosso, How to exploit the full potential of the dip-coating process to better control film formation, Journal of Materials Chemistry, 21 (2011) 17033-17038.
[25] Y. Wan, Zhao, On the Controllable Soft-Templating Approach to Mesoporous Silicates, Chemical Reviews, 107 (2007) 2821-2860.
[26] H.L. Castricum, A. Sah, R. Kreiter, D.H.A. Blank, J.F. Vente, J.E. ten Elshof, Hybrid ceramic nanosieves: stabilizing nanopores with organic links, Chemical Communications, (2008) 1103-1105.
[27] D.I. Dimitrov, A. Milchev, K. Binder, Capillary Rise in Nanopores: Molecular Dynamics Evidence for the Lucas-Washburn Equation, Physical Review Letters, 99 (2007) 054501.
[28] F. Caupin, M.W. Cole, S. Balibar, J. Treiner, Absolute limit for the capillary rise of a fluid, EPL (Europhysics Letters), 82 (2008) 56004.
[29] S. Gruener, T. Hofmann, D. Wallacher, A.V. Kityk, P. Huber, Capillary rise of water in hydrophilic nanopores, Physical Review E, 79 (2009) 067301.
[30] C. Bakli, S. Chakraborty, Capillary filling dynamics of water in nanopores, Applied Physics Letters, 101 (2012) -.
[31] D. Ortiz-Young, H.-C. Chiu, S. Kim, K. Voïtchovsky, E. Riedo, The interplay between apparent viscosity and wettability in nanoconfined water, Nat Commun, 4 (2013) 1.
[32] C.X.C. Lin, L.P. Ding, S. Smart, J.C. Diniz da Costa, Cobalt oxide silica membranes for desalination, Journal of Colloid and Interface Science, 368 (2012) 70-76.
[33] T.-D. Li, J. Gao, R. Szoszkiewicz, U. Landman, E. Riedo, Structured and viscous water in subnanometer gaps, Physical Review B, 75 (2007) 115415.
[34] A.J. Burggraaf, Transport and separation properties of of membranes with gases and vapours, in: A.J. Burggraaf, L. Cot (Eds.) Fundamentals of Inorganic Membrane Science and Technology, Elsevier, Amsterdam, 1996, pp. 331-433.
[35] A.W. Thornton, T. Hilder, A.J. Hill, J.M. Hill, Predicting gas diffusion regime within pores of different size, shape and composition, Journal of Membrane Science, 336 (2009) 101-108.
[36] B.S. Sparrow, Empirical equations for the thermodynamic properties of aqueous sodium chloride, Desalination, 159 (2003) 161-170.

[37] R.B. Evans, G.M. Watson, E.A. Mason, Gaseous Diffusion in Porous Media. II. Effect of Pressure Gradients, The Journal of Chemical Physics, 36 (1962) 1894-1902.
[38] R.B. Evans, G.M. Watson, E.A. Mason, Gaseous Diffusion in Porous Media at Uniform Pressure, The Journal of Chemical Physics, 35 (1961) 2076-2083.
[39] X. Gao, M.R. Bonilla, J.C.D.d. Costa, S.K. Bhatia, The transport of gases in macroporous α-alumina supports, Journal of Membrane Science, 409–410 (2012) 24-33.
[40] G. Ji, G. Wang, K. Hooman, S. Bhatia, J.C. Diniz da Costa, Simulation of binary gas separation through multi-tube molecular sieving membranes at high temperatures, Chemical Engineering Journal, 218 (2013) 394-404.
[41] G. Ji, G. Wang, K. Hooman, S. Bhatia, J.C. Diniz da Costa, Scale-Up Design Analysis and Modelling of Cobalt Oxide Silica Membrane Module for Hydrogen Processing, Processes, 1 (2013) 49-66.
[42] M. Elma, C. Yacou, J. Diniz da Costa, D. Wang, Performance and Long Term Stability of Mesoporous Silica Membranes for Desalination, Membranes, 3 (2013) 136-150.
[43] F.P. Incropera, D.P. DeWitt, Fundamentals of heat and mass transfer, John Wiley & Sons, New York, 1996.
[44] R.M. de Vos, W.F. Maier, H. Verweij, Hydrophobic silica membranes for gas separation, Journal of Membrane Science, 158 (1999) 277-288.
[45] M. Antognozzi, A.D.L. Humphris, M.J. Miles, Observation of molecular layering in a confined water film and study of the layers viscoelastic properties, Applied Physics Letters, 78 (2001) 300-302.
[46] Y. Zhu, S. Granick, Viscosity of Interfacial Water, Physical Review Letters, 87 (2001) 096104.
[47] S.H. Khan, G. Matei, S. Patil, P.M. Hoffmann, Dynamic Solidification in Nanoconfined Water Films, Physical Review Letters, 105 (2010) 106101.
[48] M.P. Goertz, J.E. Houston, X.Y. Zhu, Hydrophilicity and the Viscosity of Interfacial Water, Langmuir, 23 (2007) 5491-5497.

Abbreviation:

CP	Concentration polarization
EDX	Energy Dispersive X-ray Spectroscopy
EISA	Evaporation-induced self-assembly
LEP	Liquid entry pressure
MD	Membrane distillation
TP	Temperature polarization
VMD	Vacuum membrane distillation

Symbols:

$C_{p,l}$	Specific heat of water, J kg^{-1} K^{-1}
D	Diffusion coefficient
H	Enthalpy, J
J_m	Mass flux kg m^{-2} s^{-1}
k_B	Boltzmann constant, m^2 kg s^{-2} K^{-1}
k_l	thermal conductivity of liquid phase, J m^{-1} s^{-1} K^{-1}
k_s	thermal conductivity of vapour and substrate
r_s	pore radius of substrate, nm
$\overline{P}$	mean pressure within the membrane pores
Q	heat loss, J m^{-2}
T	absolute temperature, K

Greek symbols:

ε	porosity of membrane

δ	thickness
τ	tortuosity of membrane pore
γ	liquid surface tension
θ	contact angle
η	viscosity
λ	mean free path
σ	collision diameter
ρ	density

Subscript:

il	interlayer
if	interface
l	liquid phase
v	vapour phase

Highlights

- Hydrophilic nanoporous organosilica membrane successfully demonstrated for VMD
- Theoretical model proposed to describe water transport includes capillary flow
- Model accounts for increased shear viscosity of water in nano-confined spaces.
- Hydrophilic pores with $d_p < 3$ nm offer good water flux and minimal water intrusion.